Sensors and Materials, Vol. 32, No. 7 (2020) 2277–2288
MYU Tokyo

S & M 2257

Importance of Pore Structure and Surface Chemistry in Carbon Dioxide Adsorption on Electrospun Carbon Nanofibers

Yu-Chun Chiang,[1,2*] Shang-Tse Lee,[1] Yan-Juin Leo,[1] and Te-Lung Tseng[1]

[1]Department of Mechanical Engineering, Yuan Ze University,
135 Yuan-Tung Rd., Chung-Li, Taoyuan 32003, Taiwan
[2]Fuel Cell Center, Yuan Ze University, 135 Yuan-Tung Rd., Chung-Li, Taoyuan 32003, Taiwan

(Received April 16, 2019; accepted May 20, 2020)

Keywords: carbon nanofiber, adsorption, carbon dioxide, carbonization

The development of carbon dioxide (CO_2) capture technology is of great urgency for reducing the emission of CO_2 to the atmosphere and mitigating global warming. Polyacrylonitrile-based electrospun carbon nanofibers were prepared in this study at different carbonization temperatures for CO_2 capture. The effects of the primary surface features and the functional groups of the carbon nanofibers on CO_2 adsorption capacity were discussed. Results showed that the carbonization temperature influenced the porous texture and the surface chemical states of the carbon nanofibers significantly. The specific surface area, total pore volume, and micropore volume of the fibers increased with increasing carbonization temperature, but the ultra-micropore volume presented a different trend. The samples carbonized at 750 °C had the smallest average pore hydraulic radius. Moreover, in the micropore range, the volume of sub-micropores increased at a greater rate than that of ultra-micropores after activation. The carbonization temperature was also of great importance in controlling the nitrogen content and composition. A CO_2 uptake of 3.47 mmol/g at 25 °C and 1 atm was achieved. The ultra-micropore volume of the carbon nanofibers was the most important parameter for determining CO_2 uptake at 1 atm; however, the CO_2 adsorption capacity at 0.15 atm was highly dependent on the surface pyrrolic or pyridonic groups.

1. Introduction

The combustion of fossil fuels has resulted in the significant release of carbon dioxide (CO_2) to the atmosphere, which has been regarded as a major contributor to global warming. Since the dependence on fossil fuels still cannot be avoided, CO_2 emission control is of vital importance. Many studies have been dedicated to developing carbon capture and sequestration technologies to reduce the emission of CO_2 to the atmosphere.[1,2] Currently, absorption–regeneration technologies using amine-based or ammonia-based absorbents are being used in most large-scale commercialized CO_2 capture systems. Absorption is an effective method for CO_2 capture, but it is accompanied by high energy demand during the regeneration process,

*Corresponding author: e-mail: ycchiang@saturn.yzu.edu.tw
https://doi.org/10.18494/SAM.2020.2871

ISSN 0914-4935

corrosion problems, oxidative degradation of the amines, and flow problems caused by viscosity, compelling industry to look for alternative technologies for the removal of CO_2.[3]

Recently, there has been high interest in studies of CO_2 adsorption on porous solid materials. However, the optimization of porous adsorbents for CO_2 capture is still in progress. The CO_2 adsorption performance is highly influenced by the porous structure and surface functional groups of adsorbents. Hu *et al.*[4] found that pores smaller than 1 nm in diameter were the main contributors to high CO_2 uptake at atmospheric pressure. These pores with diameters smaller than 1 nm can be controlled via the activation conditions. Presser *et al.*[5] reported that pores smaller than 0.5 nm contributed the most to the CO_2 uptake at 0.1 bar, and pores smaller than 0.8 nm contributed the most at 1 bar. de Souza *et al.*[6] showed that the CO_2 uptake increased linearly with the volume of pores smaller than 0.7 nm. Wickramaratne and Jaroniec[7] observed that a high CO_2 capacity of 8.9 mmol/g at 0 °C and 1 bar on activated phenolic resin–derived carbon spheres was primarily due to the presence of small micropores (<0.8 nm).

The incorporation of different nitrogen-containing functional groups onto the surface of porous solid adsorbents is the most commonly used method to improve CO_2 uptake.[8,9] Nitrogen enrichment can effectively introduce basic functionalities, hence enhancing the specific adsorbent–adsorbate interactions for CO_2 molecules.[10] The nitrogen groups on the adsorbents having a basic character were amine groups and imine groups, so the presence of these groups should lead to higher CO_2 capacities, probably partially due to chemisorption.[11] Most studies utilized acid–base interactions to explain the high CO_2 uptake on N-doped carbons, while Xing *et al.*[12] reported another viewpoint in which the hydrogen-bonding interactions between the CO_2 molecules and the carbon surface accounted for the high CO_2 adsorption on N-doped carbons.

Activated carbon, activated carbon fibers, carbon nanofibers, zeolites, metal organic frameworks, zeolitic imidazolate frameworks, silica adsorbents, and carbon nanotubes have been intensively investigated as potential candidates for CO_2 capture. Among these porous materials, carbon nanofibers have shown several advantages over other adsorbents, such as a more concentrated pore size distribution, rapid adsorption rate, short transit distance, excellent adsorption capacity at a low concentration of adsorbates, and a low pressure drop.[13] Compared with conventional activated carbon fibers, activated carbon nanofibers possess more homogeneous and shallower pores.[14]

Several process techniques such as electrospinning, self-assembly, phase separation, template synthesis, and drawing have been applied to synthesize polymer nanofibers.[15] Among them, the electrospinning method is a very versatile and efficient technique for fabricating nano- to microscale fibers, which have much smaller diameters than conventional carbon fibers. The average fiber diameter increased with increasing polymer concentration in the precursor solution.[16,17] Xiong *et al.*[18] prepared polyacrylonitrile (PAN) nanofibers activated at a relatively low activation temperature (500 °C), with a high N content of 20.9 wt.% and a CO_2 uptake of 2.25 mmol/g at 1 bar. The pores mainly developed during carbonization and activation, and the surface chemistry was also strongly related to the conditions used for carbonization and activation.[16,19] Although the effect of the carbonization temperature of carbon nanofibers has been discussed in some studies, the activation process after carbonization was not conducted in these studies.[20] Therefore, in this study, we prepared activated PAN

carbon nanofibers by electrospinning followed by stabilization, carbonization, and activation, and we focused on the effect of the carbonization temperature on the properties and CO_2 adsorption performance of the samples. PAN was selected as the carbon precursor because it is one of the most widely used polymers for preparing carbon fibers and has a high nitrogen content and excellent thermal and mechanical properties. The properties of the samples were characterized using several techniques, and the CO_2 adsorption on the adsorbents was evaluated. Moreover, the major parameters determining the CO_2 uptake were examined statistically.

2. Materials and Methods

2.1 Sample preparation

Activated carbon nanofibers were synthesized by electrospinning. A 10 wt.% polymer solution was prepared by dissolving PAN (*MW* = 150000 g/mol, Sigma-Aldrich) in *N*, *N*-dimethylacetamide (DMAc, Sigma-Aldrich) while constantly stirring at 60 °C for 24 h in order to obtain homogeneous PAN solutions, where the PAN was utilized without further purification. Then the polymer solution was loaded into a syringe with a 23-gauge spinneret. A syringe pump (NE-1000, New Era Pump Systems, Inc., USA) was used to dispense the polymer solution at a feeding rate of 1.0 ml/h. The anode of the high-voltage power supply (FES-HV30, Falco Tech Enterprise Co., Ltd, Taiwan) was clamped to a syringe needle tip, and the cathode was connected to a stainless steel cylindrical collector (∅ 15 cm). The applied voltage was 10 kV and the tip-to-collector distance was kept constant at 10 cm. Then the solution was electrospun using an electrospinning system (FES-COS, Falco Tech Enterprise Co., Ltd, Taiwan). The electrospun nanofibers were collected on a cylindrical collector (300 rpm) covered with aluminum foil. The as-spun PAN fibers were stabilized in air at 280 °C for 12 h in a muffle furnace using a heating rate of 1 °C/min. The carbonization of stabilized nanofibers was conducted in a tubular furnace at four different temperatures (650, 750, 950, and 1050 °C) with a heating rate of 5 °C/min under flowing nitrogen of 100 sccm, and the temperature was maintained for 1 h. Then the carbonized fibers were activated at 850 °C for 2 h in a CO_2 atmosphere (100 sccm). CO_2 activation generates a larger pore volume percentage in the micropore range and a higher yield of the product, so CO_2 was chosen as the activating agent. The carbonized samples were labeled as NF*x*, with *x* indicating the carbonization temperature. The activated samples were denoted as NF*x*a.

2.2 Characterization

The morphology of the samples was observed by field emission scanning electron microscopy (FESEM) in a microscope (S-4700, Hitachi, Krefeld, Germany). The surface features of the samples were probed from N_2 adsorption–desorption isotherms measured at −196 °C using an accelerated surface area and porosimetry (ASAP) apparatus (ASAP2020, Micromeritics, Norcross, GA, USA). The specific surface areas of the samples were measured at relative pressure (P/P_o) = 0.05–0.3 by the Brunauer–Emmett–Teller (BET) method. The

micropore (<2.0 nm) surface area (S_{mi}) was determined by the t-plot method. The single-point total pore volume (V_t) was obtained at $P/P_o \approx 0.99$. The micropore and ultra-micropore (<0.7 nm) volumes (denoted as V_{mi} and V_{ultra}, respectively) were calculated by applying the nonlocal density functional theory (NLDFT). X-ray photoelectron spectroscopy (XPS) was applied to determine the number and type of functional groups present on the surface of the samples. The XPS spectra of the samples were obtained using a spectrometer (PHI 5000 VersaProbe II, ULVAC-PHI, Kanagawa, Japan), where a scanning X-ray monochromator (Al anode, hv = 1401 eV) was used and the information on elements within a few nanometers of the sample surface could be obtained. A nonlinear least squares curve-fitting program (XPSPEAK software, version 4.1, The Chinese University of Hong Kong, Hong Kong, China) was used for the deconvolution of the XPS N_{1s} spectra.

2.3 CO_2 adsorption experiments

The CO_2 adsorption experiments were carried out on selected samples at 25, 40, or 55 °C under a CO_2 pressure of less than 120 kPa using a Micromeritics ASAP 2020 system. The CO_2 uptake was measured by the volumetric method. CO_2 gas with a high purity of 99.999% was supplied by a gas cylinder. A sample of about 0.05 g was used in experiments. In our previous work,[21] the Freundlich equation [Eq. (1)] provided a good fit to CO_2 adsorption data on carbon nanofibers, so it was used in this study to fit the adsorption isotherms of CO_2 on the selected samples accordingly.

$$q_e = K_F P^{1/n} \tag{1}$$

Here, K_F [(mmol/g)(1/kPa)$^{1/n}$] is the Freundlich adsorption coefficient and n is a constant indicating the isotherm curvature. The isosteric heat of adsorption (Q_{st}) is a measure of the interaction between adsorbate molecules and adsorbent lattice atoms and can be used as a measure of the energetic heterogeneity of a solid surface.[22] Q_{st} can be calculated by the Clausius–Clapeyron equation as follows:

$$-\frac{Q_{st}}{R} = \frac{d \ln P}{d \frac{1}{T}}, \tag{2}$$

where Q_{st} (kJ/mol) is the isosteric heat of adsorption, R (= 8.314 J/mol/K) is the gas constant, and T (K) is the adsorption temperature.

3. Results and Discussion

3.1 FESEM images

FESEM images of the samples are shown in Fig. 1. The average fiber diameters of the carbonized samples decreased from about 500 nm (NF650) to 330 nm (NF1050) with increasing

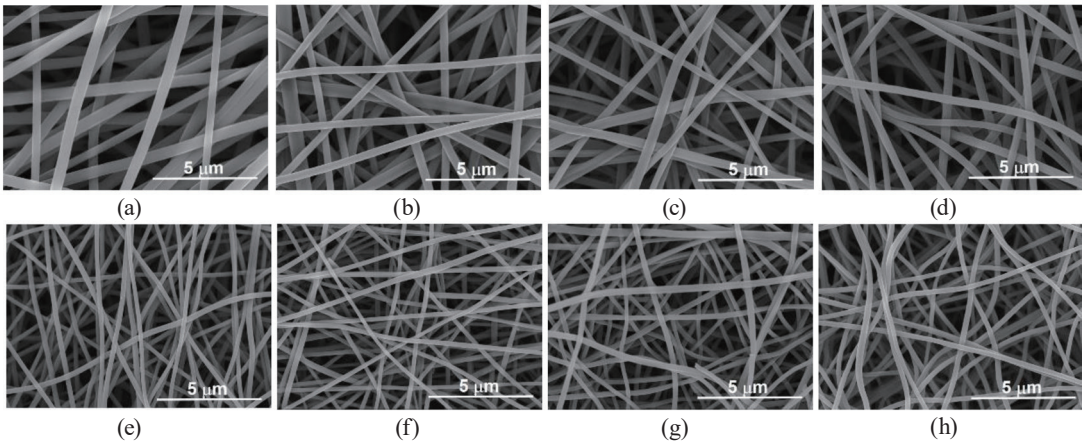

Fig. 1. FESEM images: (a) NF650; (b) NF750; (c) NF950; (d) NF1050; (e) NF650a; (f) NF750a; (g) NF950a; (h) NF1050a.

carbonization temperature. Carbonization is a process in which the material is heated in the absence of air to a temperature high enough to drive off volatile materials and produce solid porous carbon. When the carbon nanofibers were successively activated, the size of the carbon nanofibers was in the order NF750a (194 nm) < NF650a (201 nm) < NF1050a (214 nm) < NF950a (220 nm). The smaller average fiber diameters of NF650a and NF750a were attributed to their carbonization temperatures being lower than the activation temperature. It is believed that the samples carbonized at 650 and 750 °C were relatively unstable during the activation process at 850 °C because the carbonization temperature was lower than that at activation. Therefore, after activation, not only were large internal and external surface areas generated, but also a greater decrease in the fiber diameter was observed.

3.2 Surface features

The calculated surface textural properties of the samples determined from N_2 adsorption–desorption isotherms at −196 °C are summarized in Table 1, which indicates that the samples were intrinsically microporous, even the unactivated ones. The values of S_{BET}, S_{mi}, V_t, and V_{mi} generally increased with increasing carbonization temperature for both carbonized and activated samples. Furthermore, there was a noticeable increase in micropore surface area and volume after activation. However, the largest V_{ultra} occurred for NF950 among the carbonized samples and for NF650a among the activated samples. The average pore hydraulic radius was the smallest on the samples carbonized at 750 °C. After activation, the development of ultra-micropores slowed down with increasing carbonization temperature, or even the ultra-micropores expanded to sub-micropores. Among the carbonized samples, NF750 exhibited the largest ratios of micropore (as well as ultra-micropore) area and volume. After continued activation, NF750a still had the largest ratio of micropore area, but the largest ratio of micropore (as well as ultra-micropore) volume was observed for NF650a. This indicated that activation

Table 1
Surface porous properties of the samples determined by N_2 adsorption–desorption isotherms at −196 °C.

Sample	S_{BET} [(i)] (m^2/g)	S_{mi} [(ii)] (m^2/g)	V_t [(iii)] (cm^3/g)	V_{mi} [(iv)] (cm^3/g)	V_{ultra} [(iv)] (cm^3/g)	r_{MP} [(v)] (nm)	S_{mi}/S_{BET}	V_{mi}/V_t	V_{ultra}/V_t	V_{ultra}/V_{mi}
NF650	188	146	0.1108	0.0786	0.0629	0.34	0.78	0.71	0.57	0.80
NF750	306	259	0.1795	0.1567	0.1280	0.28	0.85	0.87	0.71	0.82
NF950	473	389	0.2802	0.2404	0.1829	0.32	0.82	0.86	0.65	0.76
NF1050	531	402	0.3213	0.2660	0.1705	0.30	0.76	0.83	0.53	0.64
NF650a	673	558	0.3582	0.3156	0.2276	0.47	0.83	0.88	0.64	0.72
NF750a	872	744	0.4318	0.3798	0.2233	0.45	0.85	0.88	0.52	0.59
NF950a	976	779	0.5116	0.4136	0.2122	0.49	0.80	0.81	0.41	0.51
NF1050a	1175	758	0.6142	0.4784	0.1680	0.55	0.65	0.78	0.27	0.35

[(i)]Specific surface area (S_{BET}) was determined by the BET method. [(ii)]Micropore area (S_{mi}) was obtained using the t-plot method. [(iii)]Total pore volume (V_t) represents the single-point total pore volume at $P/P_o \approx 0.99$. [(iv)]Micropore volume (V_{mi}) and ultra-micropore volume (V_{ultra}) were determined by NLDFT, where ultra-micropore was defined as a pore size less than 0.7 nm. [(v)]Average pore hydraulic radius (r_{MP}) was estimated by micropore analysis (MP).

increased the surface area and pore volume; however, this increase mainly occurred in the non-micropore range when the carbonization temperature was higher than 750 °C. Moreover, in the micropore range (<2 nm), the increase in sub-micropore (0.7–2 nm) volume was greater than that in the ultra-micropore (<0.7 nm) volume after activation.

The pore size distributions (PSDs) in the micropore range of the samples are illustrated in Fig. 2, which were obtained from NLDFT. Several models are currently available in the NLDFT model library. In this study, two of the models were compared: one was carbon slit pores (slit) and the other one was carbon pores with a heterogeneous surface (based on the two-dimensional version) (HS-2D), as shown in Fig. 2(a). The results indicated that the HS-2D NLDFT model could detect the existence of a peak at about 0.4 nm, but the slit-NLDFT model only could probe down to 0.6 nm;[23] thus, the HS-2D-NLDFT model was subsequently used. The PSD patterns of carbonized samples [Fig. 2(b)] indicated that most of the micropores for NF650 and NF1050 were concentrated in the sub-micropore range. Figure 2(c) shows the PSD patterns of activated samples, which indicated that after activation, numerous ultra-micropores were produced in NF650a but the development of sub-micropores was dominant in other activated samples.

3.3 XPS analysis

The C_{1s}, O_{1s}, and N_{1s} photoelectrons were recorded in the XPS survey scan spectra of the nanofiber samples. The surface atomic percentages and atomic ratios are listed in Table 2. The atomic percent of the N_{1s} peak decreased with increasing carbonization temperature, and activation led to a significant loss in N_{1s}. Figure 3 shows a comparison of the high-resolution XPS N_{1s} spectra of carbonized and activated samples. A bimodal pattern was observed in all N_{1s} spectra. As seen from the figure, the functional groups at the peak of about 398.4 eV were unstable and were preferentially unbounded from the surface at a high temperature. The intensity ratios of the two major peaks in the XPS N_{1s} spectra ($I_{398.4}/I_{401.2}$) decreased in the order NF650 (1.71) > NF750 (1.48) > NF950 (0.56) > NF1050 (0.38) for the carbonized samples and NF750a (0.92) > NF650a (0.86) > NF950a (0.70) > NF1050a (0.4) for the activated samples.

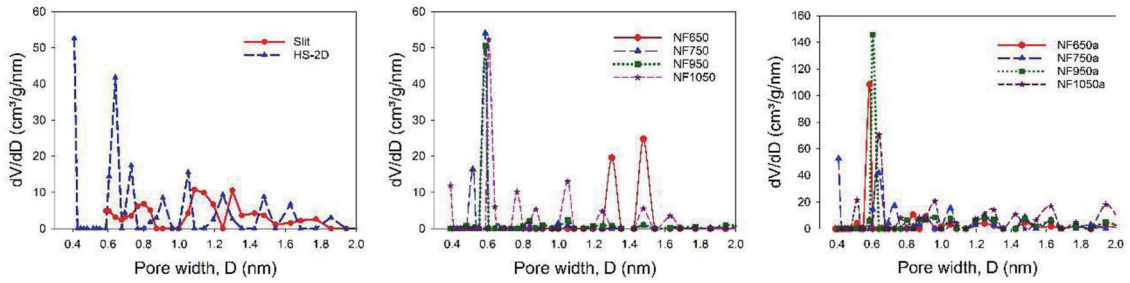

Fig. 2. (Color online) PSD of the samples. (a) Comparison of the NLDFT models in the micropore range of the samples; (b) carbonized samples; (c) activated samples.

Table 2
Surface atomic percentages and elemental ratios of the samples from XPS analysis.

Sample	Yield (%)	Atomic percent (%)			Atomic ratio	
		C_{1s}	N_{1s}	O_{1s}	O/C	N/C
NF650	52	76.5	19.9	3.6	0.047	0.260
NF750	40	81.1	15.2	3.7	0.046	0.187
NF950	28	90.6	6.4	3.0	0.034	0.070
NF1050	26	94.1	3.1	2.8	0.029	0.033
NF650a	17	88.2	7.8	4.0	0.046	0.088
NF750a	17	87.0	6.5	6.5	0.074	0.075
NF950a	15	89.3	4.9	5.8	0.065	0.054
NF1050a	11	94.7	2.8	2.5	0.027	0.029

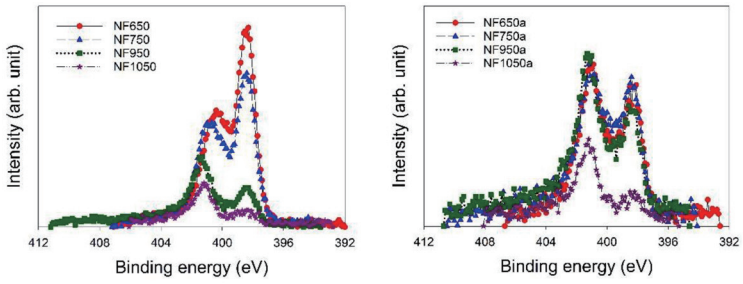

Fig. 3. (Color online) Comparison of the high-resolution XPS N_{1s} peaks: (a) carbonized samples; (b) activated samples.

The deconvolution of the high-resolution XPS N_{1s} spectra for all samples is summarized in Table 3. The N_{1s} spectra were decomposed into at most seven identified components. As seen from Table 3, the predominant group shifted from the NG2 group (NF650 and NF750) to the NG3 group (NF950) and NG4 group (NF1050) for the carbonized samples as the carbonization temperature increased. Moreover, the atomic percent of the NG3 group had a high value when the carbonization temperature was less than or equal to 950 °C. It is known that pyrrolic N functions as a polar site,[24] and the nitrogen atom in pyridonic N is positioned next to the

Table 3
Results of the fits of the XPS N_{1s} region for all samples, where values are given in at. % of total intensity.

Sample	Binding energy (eV)						
	395.7	398.4	400.1	401.2	402.4	404	405
	Aromatic N-imines (NG1)	Pyridine-type N (NG2)	Pyrrolic or pyridonic moieties (NG3)	Quaternary N (NG4)	Pyridine-N oxides (NG5)	Shake-up satellites (NG6)	NO_2 (NG7)
NF650	1	49	26	12	9	—	3
NF750	3	43	22	19	10	—	3
NF950	1	14	25	22	9	—	30
NF1050	4	20	11	30	27	2	5
NF650a	7	29	18	24	16	1	5
NF750a	4	30	18	19	9	1	19
NF950a	3	26	10	23	11	—	27
NF1050a	1	25	4	32	16	2	20

–OH group such that this nitrogen atom is surrounded by more electron groups and behaves as a strong Lewis base.[25] Pyrrolic N and pyridonic N are believed to increase the CO_2 adsorption capacity. For the activated samples, the NG2 and NG4 groups were the predominant functionalities on all samples. In addition, the CO_2 activation introduced many more oxygen atoms onto the fiber surface, leading to the increase in the percentage of oxygen-bound nitrogen functionalities such as chemisorbed NO_2 (NG7).

3.4 CO_2 adsorption performance

On the basis of the fact that the four activated samples had a higher specific surface area than that of carbonized samples and NF750 exhibited the greatest microporosity, especially ultra-microporosity, the above five samples were investigated for their CO_2 adsorption performance. The CO_2 adsorption isotherms on the selected samples recorded in the pressure range of 0–120 kPa at 25 °C are compared in Fig. 4(a). At 1 atm, the CO_2 uptake decreased in the order NF750a (3.47 mmol/g) > NF650a (3.29 mmol/g) > NF950a (3.13 mmol/g) > NF1050a (2.77 mmol/g) > NF750 (2.52 mmol/g). However, at 0.15 atm (a CO_2 partial pressure typically observed in flue gases), the order was NF750 (1.109 mmol/g) > NF750a (1.009 mmol/g) > NF650a (1.008 mmol/g) > NF950a (0.779 mmol/g) > NF1050a (0.640 mmol/g). This implied that the surface area and pore volume might be major contributors to the CO_2 adsorption at 1 atm, while the CO_2 adsorption capacity at 0.15 atm was controlled by the ultra-microporosity and nitrogen functionalities. The CO_2 adsorption isotherms on each sample are shown in Figs. 4(b)–4(f). The amount of adsorbed CO_2 decreased with increasing adsorption temperature, indicating that CO_2 adsorption on the samples was an exothermic reaction. The curves fitted using the Freundlich equation are also plotted in Fig. 4, which almost overlap with the experimental data. Consequently, the Freundlich equation provided a satisfactory fit for the CO_2 uptakes on the carbon nanofiber samples, with R^2 exceeding 0.997. Compared with previously reported carbon nanofibers prepared under similar conditions (Table 4), the CO_2 adsorption capacities on the samples prepared in this study showed satisfactory performance.

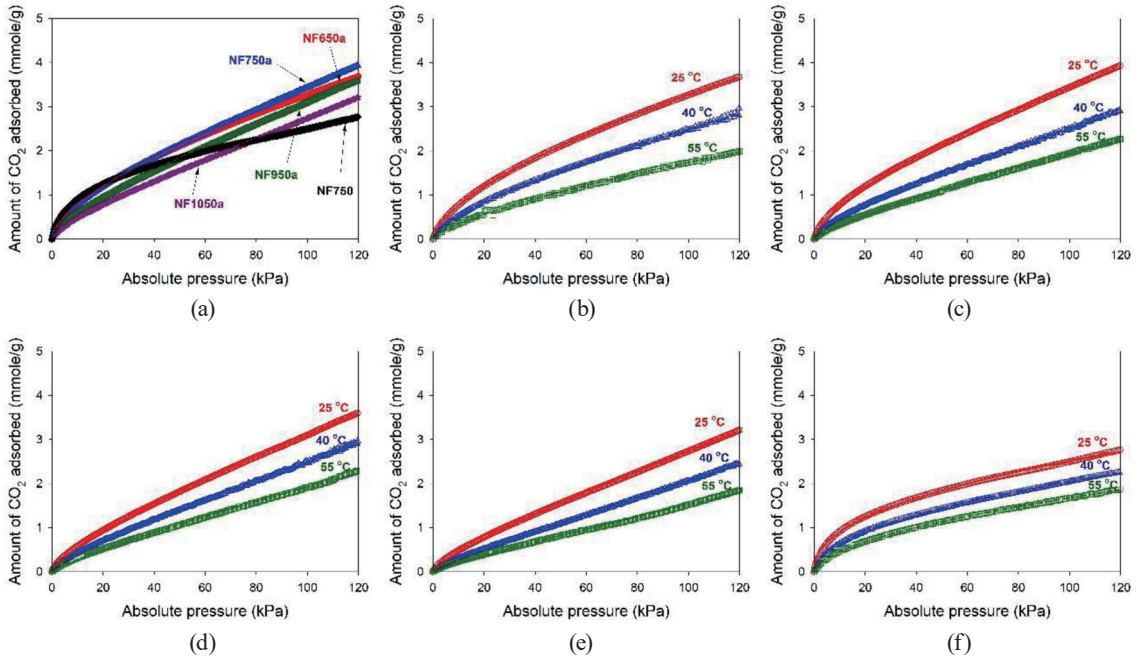

Fig. 4. (Color online) Adsorption isotherms of CO_2 of the samples: (a) all samples at 25 °C; (b) NF650a; (c) NF750a; (d) NF950a; (e) NF1050a; (f) NF750.

Table 4
Comparison of CO_2 uptake on the adsorbents in this study with various support materials prepared using electrospinning in the literature.

Adsorbent	Precursor	S_{BET} (m^2/g)	Conc. of CO_2	Temp. (°C)	CO_2 uptake (mmol/g)	Reference
ACNF[(i)]	PAN	872	1 atm 0.15 atm	25	3.47 1.01	This study
CNF[(ii)]	PAN	306	1 atm 0.15 atm	25	2.52 1.11	This study
ACNF	PAN	486	1 bar 0.15 bar	25	2.25 1.09	(18)
CNF	PAN	12	1 bar	25	0.55	(26)
ACNF	PAN polyvinylidene fluoride	925	1 bar	25	2.21	(26)
ACNF	PAN	412	1 bar	25	0.92	(27)
ACNF	PAN melamine	547	1 bar	25	1.44	(27)
CNF	PAN	966	1 bar	25	2.9	(20)
ACNF	PAN	897	1 atm 0.15 atm	25	3.17 1.00	(21)

[(i)]ACNF represents activated carbon nanofibers. [(ii)]CNF means carbonized carbon nanofibers.

The relationship between the amount of adsorbed CO_2 and the Q_{st} value is shown in Fig. 5. As can be seen from the figure, Q_{st} decreased log-linearly with increasing CO_2 loading from 0.1 to 1.2 mmol/g, which indicated that the interactions between CO_2 molecules and the pore walls of the adsorbents were stronger than those between CO_2 molecules.[(28)] Moreover,

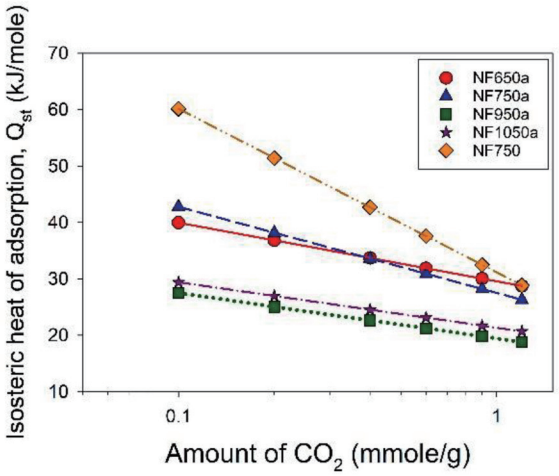

Fig. 5. (Color online) Isosteric heat of adsorption (Q_{st}) of CO_2 on the samples.

the variation of Q_{st} with the surface loading also revealed that the active sites on the surface of activated carbon nanofibers for CO_2 adsorption were energetically heterogeneous. This means that different levels of surface energy existed.[29] The Q_{st} values were higher at low CO_2 loading, which was attributed to the interactions between CO_2 molecules and the basic nitrogen functionalities or the enhanced micropore confinement.[30] The CO_2 adsorption on the samples in this study involved physical adsorption.

NF750a, possessing a relatively low specific surface area, displayed the highest CO_2 uptake at 25 °C and 1 atm. On the other hand, NF950a and NF1050a had larger specific surface areas and exhibited lower CO_2 adsorption capacities. This indicated that some other factors control the CO_2 adsorption in addition to the specific surface area.[8] In order to determine the effect of the adsorption parameters on CO_2 adsorption on carbon nanofibers, correlation analysis was carried out. The parameters with a high correlation coefficient with the CO_2 uptake were selected to conduct regression analysis, and the regression equation with the highest R^2 was considered as the optimal model. The results are summarized in Table 5. When the amounts of adsorbed CO_2 at 0.15 and 1 atm were both considered, the main factors affecting adsorption capacity were the CO_2 pressure and adsorption temperature. At a CO_2 pressure of 1 atm, the key parameters were V_{ultra} and the adsorption temperature, but the dominant factors were pyrrolic or pyridonic groups and the adsorption temperature at a CO_2 pressure of 0.15 atm. Excluding the effect of the adsorption temperature, at a CO_2 pressure of 0.15 atm, V_{ultra} and the pyrrolic or pyridonic groups were the crucial parameters at 25 and 40 °C, but at 55 °C, the N_{1s} content was the only significant factor. At a CO_2 pressure of 1 atm, although V_{ultra} remained the main factor for CO_2 adsorption at 25 and 40 °C, the major parameter shifted to O_{1s} for CO_2 adsorption at 55 °C. As a consequence, the CO_2 uptake was highly associated with V_{ultra} at 1 atm and the pyrrolic or pyridonic groups at 0.15 atm at room temperature, in addition to the CO_2 pressure and adsorption temperature.

Table 5
Regression models of the amount of CO_2 adsorption amount (mmol/g) as functions of the parameters.

CO_2 pressure (atm)	Temperature (°C)	Model	$R^2_{adjusted}$ (%)
0.15, 1	25, 40, 55	$q_e = 9.32 + 2.02\ P - 0.0286\ T$	92.0
1	25, 40, 55	$q_e = 14.4 - 0.0420\ T + 5.64\ V_{ultra}$	93.2
0.15	25, 40, 55	$q_e = 5.30 - 0.0153\ T + 0.103\ [N_{400.1\ eV}]$	88.9
1	25	$q_e = 1.35 + 8.78\ V_{ultra}$	91.3
	40	$q_e = 1.31 + 5.33\ V_{ultra}$	84.1
	55	$q_e = 1.27 + 0.111\ [O_{1s}]$	98.1
0.15	25	$q_e = 0.175 + 2.59\ V_{ultra} + 0.180\ [N_{400.1\ eV}]$	95.8
	40	$q_e = 0.138 + 1.62\ V_{ultra} + 0.133\ [N_{400.1\ eV}]$	97.8
	55	$q_e = 0.305 + 0.0198\ [N_{1s}]$	89.4

*q_e: CO_2 adsorption amount (mmol/g), P: CO_2 pressure (atm), T: temperature (°C), V_{ultra}: ultra-micropore volume (cm^3/g), $[N_{400.1\ eV}]$: atomic ratio of the nitrogen functional groups at binding energy = 400.1 eV, $[O_{1s}]$ and $[N_{1s}]$: atomic percentages of surface O_{1s} and N_{1s} peaks, respectively.

4. Conclusions

PAN-based carbon nanofibers were successfully prepared by electrospinning, with average fiber diameters ranging from 194 to 220 nm (activated) and from 330 to 500 nm (only carbonized), large specific surface areas, micropores and ultra-micropores, and high nitrogen contents. It was observed that the carbonization temperature determined the PSD, as well as the predominant type and the distribution of surface nitrogen functionalities. A high carbonization temperature resulted in a lower N content of the fibers, and the effect of successive activations depended on the carbonization temperature. The highest CO_2 adsorption capacity at 25 °C and 1 atm was observed on the samples carbonized at 750 °C followed by physical activation, which was the synergetic outcome of several physical and chemical properties of the adsorbents, which were highly dependent on the preparation conditions. Statistical relationships between the CO_2 uptake and the highly associated parameters have been established in this study.

Acknowledgments

This work was supported by the Ministry of Science and Technology of Taiwan (grant numbers MOST 106-2221-E-155-007-; MOST 108-2731-M-007-001-).

References

1 S. Y. Lee, and S. J. Park: J. Colloid Interface Sci. **24** (2013) 230.
2 M. Udin Harun Al Rasyid, I.U. Nadhori, A. Sudarsono, and Y.T. Alnovinda: Int. J. Eng. Technol. Innovat. **6** (2016) 79.
3 A. Houshmand, M.S. Shafeeyan, A. Arami-Niya, and W.M.A.W. Daud: J. Taiwan Inst. Chem. E. **44** (2013) 774.
4 X. Hu, M. Radosz, K.A. Cychosz, and M. Thommes: Environ. Sci. Technol. **45** (2011) 7068.
5 V. Presser, J. McDonough, S.H. Yeon, and Y. Gogotsi: Energ. Environ. Sci. **44** (2011) 3059.
6 K. C. de Souza, N. P. Wickramaratne, A. S. Ello, M. J. F. Costa, C. E. F. da Costa, and M. Jaroniec: Carbon **65** (2013) 334.
7 N. P. Wickramaratne and M. Jaroniec: J. Mater. Chem. A **1** (2013) 112.

8 X. Li, Z. Y. Sui, Y. N. Sun, P. W. Xiao, X. Y. Wang, and B. H. Han: Micropor. Mesopor. Mat. **257** (2018) 85.
9 A. Abbasi, M. M. Nasef, S. Kheawhom, R Faridi-Majidi, M. Takeshi, E. Abouzari-Lotf, and T. Choong: Radiat. Phys. Chem. **156** (2019) 58.
10 C. Pevida, T.C. Drage, and C.E. Snape: Carbon **46** (2008) 1464.
11 M. M. Maroto-Valer, Z. Tang, and Y. Zhang: Fuel Process. Technol. **86** (2005) 1487.
12 W. Xing, C. Liu, Z. Zhou, L. Zhang, J. Zhou, S. Zhuo, Z. Yan, H. Gao, G. Wang, and S. Z. Qiao: Energ. Environ. Sci. **5** (2012) 7323.
13 T. Rojek, L. Gubler, M.M. Nasef, and E. Abouzari-Lotf: Ind. Eng. Chem. Res. **56** (2017) 5925.
14 K. J. Lee, N. Shiratori, G. H. Lee, J. Miyawaki, I. Mochida, S. H. Yoon, and J. Jang: Carbon **48** (2010) 4248.
15 Z. M. Huang, Y. Z. Zhang, M. Kotaki, and S. Ramakrishna: Compos. Sci. Technol. **63** (2003) 2223.
16 H. Tavanai, R. Jalili, and M. Morshed: Surf. Interface Anal. **41** (2009) 814.
17 B. I. Waisi, S. S. Manickam, N. E. Benes, A. Nijmeijer, and J. R. McCutcheon: Ind. Eng. Chem. Res. **58** (2019) 4084.
18 L. Xiong, X. F. Wang, L. Li, L. Jin, Y. G. Zhang, S. L. Song, and R. P. Liu: Energ. Fuel. (in press).
19 Y. C. Chiang, C. Y. Yeh, and C. H. Weng: Appl. Sci.-Basel **9** (2019) 1977.
20 R. Ojeda-López, J. M. Esparza-Schulz, I. J. Pérez-Hermosillo, A. Hernández-Gordillo, and A. Domínguez-Ortiz: Fibers **7** (2019) 81.
21 Y. C. Chiang, C. Y. Wu, and Y. J. Chen: Sep. Purif. Technol. **233** (2020) 116040.
22 J. S. Lee, J. H. Kim, J. T. Kim, J. K. Suh, J. M. Lee, and C. H. Lee: J. Chem. Eng. Data **47** (2002) 1237.
23 J. Jagiello, J. Kenvin, A. Celzard, and V. Fierro: Carbon **144** (2019) 206.
24 G. P. Hao, W. C. Li, D. Qian, and A. H. Lu: Adv. Mater. **22** (2010) 853.
25 X. Fan, L. Zhang, G. Zhang, Z. Shu, and J. Shi: Carbon **61** (2013) 423.
26 Y. J. Heo, Y. Zhang, K. Y. Rhee, and S. J. Park: Composites B **156** (2019) 95.
27 D. Jeong, W. Jie, A. A. Adelodun, S. Kim, and Y. Jo: J. Appl. Polym. Sci. **136** (2019) 47747.
28 B. Zhang, J. Yan, and Z. Wang: J. Phys. Chem. C **122** (2018) 12831.
29 P. Ning, F. Li, H. Yi, X. Tang, J. Peng, Y. Li, D. He, and H. Deng: Sep. Purif. Technol. **98** (2012) 321.
30 J. W. F. To, J. He, J. Mei, R. Haghpanah, Z. Chen, and T. Kurosawa: J. Am. Chem. Soc. **38** (2016) 1001.